Quasi-10-day wave and semi-diurnal tide nonlinear interactions during the southern hemispheric SSW 2019 observed in the northern hemispheric mesosphere

Maosheng He[1], Jorge L. Chau[1], Jeffrey M. Forbes [2], Denise Thorsen[3], Guozhu Li[4], Tarique Adnan Siddiqui [1],Yosuke Yamazaki[5], Wayne K. Hocking[6]

[1]Leibniz-Institute of Atmospheric Physics at the Rostock University, Kühlungsborn, Germany
[2]Ann & H.J. Smead Department of Aerospace Engineering Sciences, University of Colorado, Boulder, USA
[3]Department of Electrical and Computer Engineering, University of Alaska Fairbanks, Fairbanks, Alaska, USA
[4]Key Laboratory of Earth and Planetary Physics, Institute of Geology and Geophysics, Chinese Academy of Sciences, Beijing, China
[5]GFZ German Research Centre for Geosciences, Potsdam, Germany
[6]University of Western Ontario, 1151 Richmond St. London, Ontario, Canada N6A3K7

Key Points:

- Mesospheric winds from multiple longitudes in the NH are combined to diagnose zonal wavenumbers of waves during the Antarctic SSW 2019.
- Diagnosed are Q6DW, Q10DW, M2, SW1, SW2, SW3, and LSB and USB of Q10DW-SW2 nonlinear interactions.
- LSB and USB are generated asynchronously, during which their parent waves evolve following the Manley-Rowe energy relations.

Corresponding author: He, M., `he@iap-kborn.de`

Abstract

Mesospheric winds from three longitudinal sectors at about 65°N and 54°N latitude are combined to diagnose the zonal wavenumbers (m) of high-frequency-resolved spectral wave signatures during the rare southern hemisphere sudden stratospheric warming (SSW) of 2019. Diagnosed are quasi-10- and 6-day planetary waves (Q10DW and Q6DW, m=1), solar semi-diurnal tides with m=1, 2, 3 (SW1, SW2, and SW3), lunar semi-diurnal tide, and the upper and lower sidebands (USB and LSB, m=1 and 3) of Q10DW-SW2 nonlinear interaction. We further present a 7-year composite analysis to distinguish SSW effects from climatological behaviors. Immediately before (after) the SSW onset, LSB (USB) enhances, accompanied by the enhancing (fading) Q10DW, and a weakening of climatological SW2 maximum. These behaviors are explained in terms of Manley-Rowe energy relation, i.e., the energy goes first from SW2 to Q10DW and LSB, and then from SW2 and Q10DW to USB.

Plain Language Summary

Sudden stratospheric warming events occur typically over the winter Arctic and are well-known for being accompanied by diverse waves. A rare SSW occurred in the southern hemisphere in September 2019. Here, we combine mesospheric observations from the northern hemisphere to study the wave activities before and during the warming event. A dual-station approach is implemented on high-frequency-resolved spectral peaks to diagnose the horizontal scales of the dominant waves. Diagnosed are multiple tidal components, multiple Rossby normal modes, and two secondary waves arising from nonlinear interactions between a tide component and a Rossby wave. Most of these waves do not occur in a climatological sense and occur around the warming onset. Furthermore, the evolution of these waves can be explained using theoretical energy arguments.

1 Introduction

In the winter polar atmosphere, upward propagating Rossby waves (RWs, also called planetary waves), e.g., triggered by topography and the horizontal thermal gradient of the land-sea distribution. Such interactions may interact with the polar vortex and heat the stratosphere rapidly, known as sudden stratospheric warming events (SSWs, e.g., Butler et al., 2015). Associated with SSWs are oscillations in the middle and upper atmosphere in both neutral and plasma properties, such as the neutral density and composition, temperature, wind, plasma density, and electric current density (e.g., Chau et al., 2009; Goncharenko & Zhang, 2008; Pedatella & Forbes, 2010; He & Chau, 2019).

In the mesosphere, planetary-scale oscillations during SSWs can be categorized into two temporal scales, longer and shorter than one day, termed hereafter as RW- and tide-like oscillations, respectively. RW-like oscillations occur at periods from a few days to a few tens of days, mostly explained as RW normal modes (RNMs, e.g., Madden, 1979; Forbes, 1995). RNMs are westward-propagating and occur with wave periods near 2, 6, 10, 16, and days, and are often referred to as quasi-2-, 6-, 10-, 16-, and 28-day waves (Q2DW, Q6DW, Q10DW, Q16DW, and Q28DW, e.g., Forbes et al., 2017, 2020; Yamazaki, 2018; Zhao et al., 2019). Associations between RNMs and SSWs have also been broadly reported, although the underlying mechanisms are still under debate (e.g., He, Yamazaki, et al., 2020; Pancheva et al., 2008; Stray et al., 2015; Yamazaki & Matthias, 2019). Besides RNMs, secondary waves of nonlinear interactions between RNMs and stationary RWs are also observed during SSWs (e.g., He, Yamazaki, et al., 2020).

Oscillations, occurring around the periods of harmonics of the solar or lunar day, are explained mostly as signatures of harmonics of solar or lunar tides. Oscillations of this nature are reported to be associated with or impacted by SSWs, such as the first six solar migrating tidal harmonics (at 24hr, 12hr, ..., 4hr) and the second lunar migrating tidal harmonic (M2, at 12.4hr) (e.g., He, Forbes, et al., 2020; Chau et al., 2015; He & Chau, 2019). Among these oscillations, the sun-synchronous (migrating tide-like) components are typically explained in terms of SSW modulations of tidal heating (e.g., Goncharenko et al., 2012; Limpasuvan et al., 2016; Siddiqui et al., 2020) and of propagation conditions (e.g., He, Forbes, et al., 2020), whereas the non-sun-synchronous (non-migrating tide-like) components are conventionally explained as arising from zonal asymmetries in heating, or nonlinear interactions between stationary RWs and migrating tides (e.g., He et al., 2017; Forbes et al., 2020). Nonlinear interactions could also occur between RNMs

and tides (e.g., Forbes et al., 2020; He et al., 2017), generating secondary waves at frequencies slightly below and above the tidal frequencies, termed hereafter as lower and upper sidebands (LSBs and USBs), respectively. LSBs and USBs are often misinterpreted as tides according to He and Chau (2019).

Most knowledge of the above mesospheric wave activities is based on SSWs that occurred in the northern hemisphere (NH). In September 2019, an SSW occurred (Lim et al., 2020) in the southern hemisphere (SH), providing a unique opportunity to investigate the response of the NH middle and upper atmosphere to SH SSWs. Using Aura Microwave Limb Sounder (MLS) observations and Swarm plasma and magnetic observations, Yamazaki et al. (2020) revealed 6-day periodicities in the middle atmosphere and ionosphere. Conventionally, such like periodicities were explained most often as Q6DW. However, a recent modeling study (Miyoshi & Yamazaki, 2020) suggested that the ionospheric 6-day periodicities in the 2019 case might not be Q6DW signatures but aliases from near-12hr waves resulted from Q6DW-SW2 nonlinear interaction. This aliasing, between RNWs and their secondary waves associated with migrating tides, is an inherent sampling property of all quasi-sun-synchronous single-spacecraft missions, which is explained mathematically in Appendix A. The current work uses ground-based observations to eliminate the concerns about the aliasing and investigate the potential RNMs and near-12hr waves. Implementing a dual-station approach, we are also able to diagnose zonal wavenumbers of the underlying waves, beyond the capabilities of single-station approaches. Our results illustrate the presence of both RNMs and near-12h waves in the mesosphere, and reveal how the Q10DW-tidal interactions result in the mesospheric wind variability during the SH SSW.

2 Observation and method

The current work uses five radar systems, at Juliusruh (13.4°E, 54.6°N), Mohe (122°E, 53.5°N), Andenes(16.0°E, 69.3°N), PokerFlat (147.5°W,65.1°N), and Yellowknife (114.3°W, 62.5°N), referred hereafter as J, M, A, P and Y radars, respectively. The details of the radar setups, e.g., frequencies and antenna configurations, were introduced in Hoffmann et al. (2010); Yu et al. (2013); Singer et al. (2013); Klemm (2019); Kumar and Hocking (2010), respectively. As illustrated by two dashed lines in Figure S1 in Supporting information (SI), these radars distribute largely along two latitudes, 65°N and 54°N. The zonal and meridional wind observations (u and v) around the SSW, between 1 June and

31 November 2019 (except at Yellowknife where data is not available before 13 August), are derived between 80km and 100km altitude for a case study. As a reference and for comparison, 7-year (2012-2018) observations at Mohe and Juliusruh are also used for a composite analysis (CA).

Our main approach is the so-called phase differencing technique (PDT), developed in He, Chau, Stober, et al. (2018) and has been explained mathematically and implemented several times (e.g., He, Chau, Hall, et al., 2018). Here, we explain PDT briefly. Based on dual-point configurations, PDT makes use of the phase difference between two locations on the wave path to estimate the wavenumber in the direction defined by the two points (The same idea was also used in, e.g., the deconvolution procedure Hocking et al., 2014). When the two locations are at the same latitude, estimated would be the zonal wavenumber m. The estimation is based on two main assumptions. The first one, called single wave assumption, is that the wavenumber is a function of frequency. The other, called long wave assumption, is that the separation between the two locations is shorter than half the wavelength of the underlying wave. Particularly, in diagnosing RWs and tides, m could be assumed as a near-zero integral number, which might relax the long wave assumption from half wavelength to one and a half wavelength. PDT has been implemented, through cross-wavelet (CWL) analysis, to diagnose m of RW- and tide-like oscillations in a few NH SSWs (e.g., He, Chau, Stober, et al., 2018; He, Yamazaki, et al., 2020). Further validating PDT, different dual-station configurations at the same latitude yielded consistent results (e.g., He, Forbes, et al., 2020). The current work applies PDT to the SH SSW 2019, using three dual-radar configurations, i.e., M-J, P-A, and Y-A.

3 Results

As explained in the introduction, most planetary-scale wave activities during SSWs are RW- and tide-likes oscillations. Therefore, we explore the waves in two frequency ranges in Sections 3.1 and 3.2, respectively. Section 3.3 focuses only on $T = 12.0 \pm 0.2$hr.

3.1 Multi-day oscillations

Figure 1a presents $|\tilde{W}^J_{(f,t)}|$, a Gabor wavelet (Torrence & Compo, 1998) of the zonal wind at 95km altitude over Juliusruh. In the plot, the dashed vertical line on 08 September denotes the onset of the SH SSW 2019. The onset refers to the central day between

5-11 September, during which the atmospheric temperature at 10 hPa increased rapidly from 208K to 259K according to the MERRA2 reanalysis data (e.g., Yamazaki et al., 2020). The most dominant character of Figure 1a is the peak at periods T= 6-8 days around 1 October, as highlighted by a horizontal arrow. There is another peak around T= 10 days around 1 September, before the onset and highlighted by an arrow. Both of the 6- and 10-day peaks also occurred over Mohe, as displayed in the spectrum $|\tilde{W}^M_{(f,t)}|$ in Figure 1b. The coincidence between the two radars allows diagnosis of m through CWL analysis (readers are referred to, e.g., He, Yamazaki, et al., 2020, for details), The CWL spectrum between Figures 1a and 1b, $\tilde{C}_{(f,t)} = \tilde{W}^{J*}_{(f,t)}\tilde{W}^M_{(f,t)}$, is shown in Figure 1c, in which the darkness denotes the amplitude $|\tilde{C}|$ while the color hue denotes $Arg\{\tilde{C}\}$. $Arg\{\tilde{C}\}$ measures the phase difference of the osculations between the stations. Assuming the phase difference is due to the propagation of a dominant wave with the wavenumber m, then $Arg\{\tilde{C}\} = m\lambda_\Delta$ is a function of m and the longitudinal separation between the two radars λ_Δ. The color hue of Figure 1c is adjusted so that the redness represents $Arg\{\tilde{C}\} = \lambda_\Delta$, corresponding to m=1. In Figure 1c, both the 6- and 10-day peaks are associated with m=1, suggesting both peaks are the RNMs, i.e., Q6DW and Q10DW, respectively. Similar Q6DW and Q10DW signatures occur also at 65°N detected by the P-A radar pair, as displayed in Figure S2d in SI.

For comparison and as a reference, we present a CA in Figures 1d-f, using the data from J-M pair between 2012 and 2018. Similarly to the 2019 case, in Figures 1d-f Q6DW also occurs around 1 October, whereas Q10DW is not visible around 1 September which is different from the 2019 case.

3.2 Near-12hr oscillations

Figure 2a presents a CWL spectrum similar to Figure 1c but for the altitude-averaged spectrum at periods near 12hr. Different from Figure 1c showing the spectrum of only u, Figure 2a displays the sum of the spectra of u and v since the spectra are almost identical to each other. The black isolines denote amplitudes at $\sqrt{|\tilde{C}|}$= 8, 12, 16, and 24m/s. In Figure 2a, the most dominant peak occurs at 12.0hr, characterized by m=2 and $\sqrt{|\tilde{C}|} >$ 24m/s before the SSW onset, corresponding to the tidal component SW2. In the current work, SWm denotes semi-diurnal westward propagating component with zonal wavenumber m. In Figure 2a and at 12.4hr, as indicated by a horizontal arrow, another peak oc-

curs above $\sqrt{|\tilde{C}|} > 12$m/s. The 12.4hr peak is characterized by m=2, and therefore should be a signature of the lunar tide M2.

Figure 2b is the same plot as Figure 2a but from the radar pair A-P, at 65°N. Similarly to Figure 2a, in Figure 2b the spectrum also maximizes at 12.0hr and 12.4hr above $\sqrt{|\tilde{C}|} > 24$m/s and 12m/s, respectively. The 12.0hr peak is mostly characterized by m=2, and so is the 12.4hr peak, which therefore suggests the underlying waves are SW2 and M2, respectively. In addition, in Figure 2b and between 11.0-11.5hr, there is a dominant blue peak, maximizing at $\sqrt{|\tilde{C}|}$= 17.9m/s, at T= 11.36hr on 12 September 2019, as indicated by the white cross. However, the color of the 11.36hr is close to m=1 and =3 in the color code map, due to the special radar separation $\lambda_\Delta \approx \pi$ and $\lambda_\Delta + 2\pi \approx 3\lambda_\Delta$. To determine m, we produce the same spectra as Figure 2b but for the radar pair A-Y, displayed in Figure 2c.

Similarly to Figure 2b, Figure 2c also exhibits peaks at T= 12.4hr, 12.0hr and 11.0-11.5hr. The previous two are associated with m=2, whereas the third peak, as illustrated by the white cross, maximizes at $\sqrt{|\tilde{C}|}$= 11.1m/s, at T= 11.29hr on 14 September 2019. The blueness suggests the underlying dominant wave is associated with m=3, which is compatible with the blue peak in Figures 2b. Actually, the color codes for all panels of Figure 2 are adapted so that the blueness represents m=3. A weak blue or purple peak could also be found in Figure 2a as indicated by the white cross, maximizing at $\sqrt{|\tilde{C}|}$=9.1m/s, T=11.36hr. Additionally, in Figure 2c and immediately before the onset, a red peak occurs at T=12.73hr with $\sqrt{|\tilde{C}|}$=8.0m/s as indicated by a white cross. The redness suggests the underlying wave is associated with m=1. Similar 12.7hr peaks also occur in Figures 2b and 2a, indicated by white crosses there.

Figure 2d displays the same plot as Figure 2a but from the 7-year CA, which comprises mainly the 12.0hr peak but not the off-12.0hr peaks seen in Figures 2a-c, at least not at the comparable magnitudes. The 12.0hr peak is also different from those in Figures 2a-c, e.g., the peak exhibits a minimum in late October in Figure 2d, but prematurely around 1 October in Figure 2a. We look into the details in the next subsection.

3.3 Solar semi-diurnal tide

To investigate the 12.0hr peak, we reproduce spectra similar to Figure 2a but at every individual altitude, and then pick the values only at T=12.0±0.2hr at each altitude and combine them into the time-height plane, displayed in Figure 3a. Similarly, Fig-

ures 3b, 3c, and 3d are constructed from spectra similar to Figures 2b, 2c, and 2d. In all panels here, green represents m=2. The most dominant character in Figure 3d is the green peak (m=2), maximizing vertically at about 90km in September. The September maximum is a well-known climatological behavior (also cf., Figures 7b and 1c in He & Chau, 2019; Conte et al., 2017, respectively). The pattern around the SSW in Figure 3a could be explained as a distorted version of the climatological maximum. The maximum occurs 10-20d earlier and splits around 90km and above, in comparison with Figure 3d.

The premature and split maximum also occurs in Figures 3b and 3c, but associated with more interesting behaviors. As indicated by the horizontal arrows, blueness (or purpleness) and redness occur at h=90km and 95km, respectively. These colors suggest that the dominant underlying wave there is not SW2. In Figure 3c, blueness and redness represent m= 1 and 3, suggesting the underlying waves are the non-migrating tides, SW1 and SW3, respectively.

4 Discussions

The previous section diagnoses the zonal wavenumber m of potential waves seen in cross wavelet spectra, in two ranges of period, namely, multi-days and near-12hr. In the current section, we discuss them as RNMs, tides, and secondary waves of RNM-tide nonlinear interactions.

4.1 Association of RNMs with SH SSW

Although there are observational studies suggesting that SSWs are not associated with RNMs (e.g., Sassi et al., 2012), most observational studies support associations, at least for most NH SSWs between 2004 and 2018 (e.g., He, Yamazaki, et al., 2020; Pancheva et al., 2008; Stray et al., 2015; Yamazaki & Matthias, 2019; Gong et al., 2018; Yamazaki, 2018; Chandran et al., 2013; Manney et al., 2008). The burst of Q6DW in late September 2019 was reported by Yamazaki et al. (2020) using geopotential height (GPH) observations of Aura MLS and magnetic observations from Swarm. The 2019 Q6DW amplitude, in GPH, was stronger than the 2004-2018 average amplitude, especially above 70km altitude in SH. Consistently, our comparison between Figures 1c and 1f also illustrates that in NH the 2019 Q6DW is also stronger than the multi-year average. However, such a strong NH Q6DW in this season is not unique for 2019. Among the seven years we explored, Q6DW also occurred at comparable or even stronger amplitudes in

the same season in 2013 and 2017 (observed from the same figures as Figures 1a-c but for 2012-2018, not shown here).

In contrast to the climatological occurrence of the Q6DW, the occurrence of the Q10DW in early September is unique for 2019, and also temporally more close to the SH SSW, c.f, Figures 1a-c vs. 1d-f. Therefore, we argue that the Q10DW is potentially associated with the SSW. Consistent with our Q10DW results, the SH GPH results (Figure 3a in Yamazaki et al., 2020) also exhibited a spectral peak, not mentioned by the authors, at T= 10d around 1 September and weaker than the Q6DW amplitude by at least 50%. The consistency of our NH ground-based results with the SH satellite-based results suggests that the Q6DW and Q10DW are both active on global scales, consistent with their interpretation as RNM. Coincidentally, a Q10DW signature was also reported in the ionosphere during the SH 2002 (Mo & Zhang, 2020).

RNMs prior to NH SSW onsets could be explained in terms of in situ instability (e.g., Siskind et al., 2010; Pancheva et al., 2008), whereas the RNMs which appeared after the NH SSWs are believed to arise from different mechanisms, e.g., the zonal asymmetry of gravity wave breaking (e.g., Manney et al., 2008). Therefore, the Q10DW might be attributable to potential in situ instabilities. Supporting this hypothesis is the evolution of the meridional gradient of the quasi-geostrophic potential derived from the MLS GPH observations (Figures 3h-j in Yamazaki et al., 2020). The gradient is necessary for barotropic/baroclinic instability, even though the evolution and the instability were discussed to explain the Q6DW. Another potential mechanism of the Q10DW generation is the planetary wave amplification by stimulated tidal decay (PASTIDE, He et al., 2017) as detailed in the following subsection.

4.2 Secondary waves of Q10DW-SW2 nonlinear interactions

In Sections 3.2 and 3.3, we explained the 12.0hr and 12.4hr spectral peaks as solar and lunar tides, respectively. In the current subsection, we discuss other near-12hr peaks as the upper and lower sidebands (USB and LSB) of nonlinear interactions between SW2 and RNM, respectively.

According to the resonance conditions of wave-wave nonlinear interaction (e.g., He et al., 2017), the frequency and wavenumber of USB (LSB) are equal to the sum (difference) of their parent waves. Given that the RNMs, Q6DW, Q10DW, and Q16DW, are associated with m=1, all their USBs and LSBs of interactions with SW2 are asso-

ciated with m=3, and 1, respectively. Observational evidence with constraints of both f and m were reported for the sidebands of Q6DW and Q16DW using either ground-based or satellite observations (e.g., Forbes & Zhang, 2017; Forbes et al., 2020; He, Chau, Hall, et al., 2018; He, Chau, Stober, et al., 2018). As a reference, the theoretical periods of the USBs and LSBs of RNMs, according to the periods indicated by the arrows in Figures 1c and S1d, are calculated and displayed as the dashed horizontal arrows at the most right-side in all panels of Figure 2. Further, using the periods at the six white crosses (indexed hereafter as $k = 1, 2, ..., 6$) in Figures 2a-c, we calculate the theoretically required periods of the parent RNMs according to the resonance condition, resulting in six values T_k. Assuming all the six peaks share one parent RNM and using the spectral amplitude $w_k := |\tilde{C}_k|/ < |\tilde{C}_k| >_k$ in Figure 2, we calculate the weight average $\bar{T} :=< T_k w_k >_k$=8.6d with a deviation $\sigma(w_k(T_k - \bar{T}))$=0.4d, displayed as a vertical error bar in Figures 1c and S1. The horizontal error bar represents the corresponding weight-averaged time and its deviation, $\bar{t}$=11.1±2.2d after 00:00, on 1 September. In Figures 1c and S1d, the Q10DW peaks, in comparison with the Q6DW, are closer to the black cross in both t and T, and $\bar{T}$ overlaps the period of the Q10DW peak partially. Therefore, we argue that the Q10DW, rather than Q6DW, is more likely responsible to the sidebands, or at least contributes more.

Moreover, the temporal evolution of the Q10DW peak, together with those of the LSB, USB, and SW2, satisfies the energy requirements of Manley-Rowe relation (He et al., 2017). According to the Manley-Rowe relation, the LSB and USB are generated in two nonlinear interaction processes. In the LSB-generating interaction, the tide exports energy to both LSB and RNM, while in the USB-generating interaction, both RNM and tide contribute energy to USB. A potential circumstance occurring during the SH SSW 2019 is sketched in Figure 4. LSB-generating interaction occurs at t_L before the onset, generating or amplifying LSB and Q10DW at the cost of energy from SW2. Then, the amplified Q10DW further interacts with SW2 at t_U around the onset, in which both Q10DW and SW2 transport energy to the USB. This circumstance could explain following details of the wave evolutions around the onset in Figures 1-3, namely, (1) the Q10DW and LSB burst simultaneously before the onset; (2) the USB maximizes after the weakening of Q10DW; and meanwhile (3) the bursts of both LSB and USB are accompanied with the split September SW2 maximum as described in Section 3.3. According to the Manley-Rowe relation, the absolute net energy gains of the waves are proportional to

their frequencies, and 100% and 95% of the energy of the LSB and USB are contributed directly by SW2. Therefore, the energy deficits of SW2 could be responsible for the splitting of the SW2 maximum in Figures 3a-c.

On the other hand, Q6DW maximized in late September and is, therefore, less likely responsible for the LSB generation that occurred about 20-30 days prior.

5 Summary

The current study explores planetary-scale wave activities in the NH during the SH SSW 2019, using mesospheric winds detected with five meteor radar systems around 54°N and 65°N. We diagnose the zonal wavenumber m of wave signatures contained in cross-wavelet spectra of the observations from multiple longitudinal sectors. Spectral peaks are diagnosed at T= 5-7d, 8-10d, 12.0hr, 12.4hr, 11.2-11.5hr, and 12.6-12.8hr, associated dominantly with m= 1, 1, 2, 2, 3, and 1, which are explained as Q6DW, Q10DW, SW2, M2, and USB and LSB of Q10DW-SW2 nonlinear interaction, respectively. As a reference, a 7-year composite analysis is presented, illustrating that the SW2 pattern during the SH SSW could be explained as a premature and split climatological September maximum, and that the Q6DW during the SH SSW could be explained as an amplified climatological phenomenon. The detected periods of the Q10DW, LSB and USB signatures satisfy the resonance conditions of nonlinear interaction. In addition, the temporal variations of the Q10DW, LSB, USB and SW2, shortly before and after the SSW onset, could be explained in terms of the Manley-Rowe relation of nonlinear interactions. Our results illustrate that the Q10DW-SW2 interactions can explain the details of the mesospheric wind variabilities during the SH SSW 2019.

Acknowledgments

This work is supported by the Deutsche Forschungsgemeinschaft (DFG, German Research Foundation) under SPP 1788 (DynamicEarth) projects CH1482/1-2 (DYNAMITE-2). Jeffrey M. Forbes acknowledges support under NSF Award AGS-1630177 to the University of Colorado Boulder. Support for the Poker Flat Meteor Radar was provided by the National Science Foundation under grant AGS-1651464. The data from Mohe is provided by the Data Center for Geophysics (http://wdc.geophys.ac.cn/), National Earth System Science Data Sharing Infrastructure at BNOSE(Beijing National Observatory of Space Environment), IGGCAS (Institute of Geology and Geophysics, Chinese Academy of Sci-

ences). The post-processed data in this paper are available at the Harvard Dataverse through https://doi.org/10.7910/DVN/KL6QUL.

References

Butler, A. H., Seidel, D. J., Hardiman, S. C., Butchart, N., Birner, T., & Match, A. (2015). Defining sudden stratospheric warmings. *Bull. Am. Meteorol. Soc.*, *96*(11), 1913–1928. doi: 10.1175/BAMS-D-13-00173.1

Chandran, A., Garcia, R. R., Collins, R. L., & Chang, L. C. (2013). Secondary planetary waves in the middle and upper atmosphere following the stratospheric sudden warming event of January 2012. *Geophys. Res. Lett.*, *40*(9), 1861–1867. doi: 10.1002/grl.50373

Chau, J. L., Fejer, B. G., & Goncharenko, L. P. (2009, mar). Quiet variability of equatorial e × B drifts during a sudden stratospheric warming event. *Geophys. Res. Lett.*, *36*(5), 2–5. Retrieved from `http://doi.wiley.com/10.1029/2008GL036785` doi: 10.1029/2008GL036785

Chau, J. L., Hoffmann, P., Pedatella, N. M., Matthias, V., & Stober, G. (2015, apr). Upper mesospheric lunar tides over middle and high latitudes during sudden stratospheric warming events. *J. Geophys. Res. Sp. Phys.*, *120*(4), 3084–3096. Retrieved from `http://doi.wiley.com/10.1002/2015JA020998` doi: 10.1002/2015JA020998

Conte, J. F., Chau, J. L., Stober, G., Pedatella, N., Maute, A., Hoffmann, P., ... Murphy, D. J. (2017). Climatology of semidiurnal lunar and solar tides at middle and high latitudes: Interhemispheric comparison. *J. Geophys. Res. Sp. Phys.*, *122*(7), 7750–7760. Retrieved from `http://dx.doi.org/10.1002/2017JA024396http://onlinelibrary.wiley.com/store/10.1002/2017JA024396/asset/jgra53687.pdf?v=1{\&}t=jansn8up{\&}s=72eb34b0c842fc65e21955e9b8b7bfd8028227ee` doi: 10.1002/2017JA024396

Forbes, J. M. (1995). Tidal and planetary waves. *Geophys. Monogr. Ser.*, *87*, 67–87. Retrieved from `http://www.agu.org/books/gm/v087/GM087p0067/GM087p0067.shtml` doi: 10.1029/GM087p0067

Forbes, J. M., & Zhang, X. (2017). The quasi-6 day wave and its interactions with solar tides. *J. Geophys. Res. Sp. Phys.*, *122*(4), 4764–4776. Retrieved from `http://doi.wiley.com/10.1002/2017JA023954` doi:

10.1002/2017JA023954

Forbes, J. M., Zhang, X., Hagan, M. E., England, S. L., Liu, G., & Gasperini, F. (2017). On the Specification of Upward-Propagating Tides for ICON Science Investigations. *Space Sci. Rev.*, *212*(1-2), 697–713. Retrieved from `http://dx.doi.org/10.1007/s11214-017-0401-5` doi: 10.1007/s11214-017-0401-5

Forbes, J. M., Zhang, X., & Maute, A. (2020). Planetary wave (PW) generation in the thermosphere driven by the PWmodulated tidal spectrum. *J. Geophys. Res. Sp. Phys.*, 1–19. doi: 10.1029/2019ja027704

Goncharenko, L. P., Coster, A. J., Plumb, R. A., & Domeisen, D. I. (2012). The potential role of stratospheric ozone in the stratosphere-ionosphere coupling during stratospheric warmings. *Geophys. Res. Lett.*, *39*(8), 1–5. doi: 10.1029/2012GL051261

Goncharenko, L. P., & Zhang, S. R. (2008). Ionospheric signatures of sudden stratospheric warming: Ion temperature at middle latitude. *Geophys. Res. Lett.*, *35*(21), 4–7. doi: 10.1029/2008GL035684

Gong, Y., Ma, Z., Lv, X., Zhang, S., Zhou, Q., Aponte, N., & Sulzer, M. (2018, dec). A Study on the Quarterdiurnal Tide in the Thermosphere at Arecibo During the February 2016 Sudden Stratospheric Warming Event. *Geophys. Res. Lett.*, *45*(23), 13,142–13,149. Retrieved from `https://onlinelibrary.wiley.com/doi/abs/10.1029/2018GL080422` doi: 10.1029/2018GL080422

He, M., & Chau, J. L. (2019). Mesospheric semidiurnal tides and near-12 h waves through jointly analyzing observations of five specular meteor radars from three longitudinal sectors at boreal midlatitudes. *Atmos. Chem. Phys.*, *19*(9), 5993–6006. Retrieved from `https://www.atmos-chem-phys.net/19/5993/2019/acp-19-5993-2019.html`

He, M., Chau, J. L., Hall, C. M., Tsutsumi, M., Meek, C., & Hoffmann, P. (2018). The 16-Day Planetary Wave Triggers the SW1-Tidal-Like Signatures During 2009 Sudden Stratospheric Warming. *Geophys. Res. Lett.*, *45*(22), 12,631–12,638. Retrieved from `http://doi.wiley.com/10.1029/2018GL079798` doi: 10.1029/2018GL079798

He, M., Chau, J. L., Stober, G., Hall, C. M., Tsutsumi, M., & Hoffmann, P. (2017). Application of Manley-Rowe Relation in Analyzing Nonlinear Interactions Between Planetary Waves and the Solar Semidiurnal Tide During 2009 Sudden

Stratospheric Warming Event. *J. Geophys. Res. Sp. Phys.*, *122*(10), 10,783–10,795. Retrieved from http://dx.doi.org/10.1002/2017JA024630 doi: 10.1002/2017JA024630

He, M., Chau, J. L., Stober, G., Li, G., Ning, B., & Hoffmann, P. (2018). Relations Between Semidiurnal Tidal Variants Through Diagnosing the Zonal Wavenumber Using a Phase Differencing Technique Based on Two Ground-Based Detectors. *J. Geophys. Res. Atmos.*, *123*(8), 4015–4026. Retrieved from http://doi.wiley.com/10.1002/2018JD028400 doi: 10.1002/2018JD028400

He, M., Forbes, J. M., Chau, J. L., Li, G., Wan, W., & Korotyshkin, D. V. (2020, mar). High-Order Solar Migrating Tides Quench at SSW Onsets. *Geophys. Res. Lett.*, *47*(6). Retrieved from http://doi.wiley.com/10.1029/2019GL086778 doi: 10.1029/2019GL086778

He, M., Yamazaki, Y., Hoffmann, P., Hall, C. M., Tsutsumi, M., Li, G., & Chau, J. L. (2020). Zonal wavenumber diagnosis of Rossby wave like oscillations using paired ground based radars. *J. Geophys. Res. Atmos.*. Retrieved from https://doi.org/10.1029/2019JD031599 doi: 10.1029/2019jd031599

Hocking, W. K., Hocking, A., Hocking, D. G., & Garbanzo-Salas, M. (2014). Wind-profiler optimization using digital deconvolution procedures. *J. Atmos. Solar-Terrestrial Phys.*, *118*, 45–54. Retrieved from http://dx.doi.org/10.1016/j.jastp.2013.08.025 doi: 10.1016/j.jastp.2013.08.025

Hoffmann, P., Becker, E., Singer, W., & Placke, M. (2010). Seasonal variation of mesospheric waves at northern middle and high latitudes. *J. Atmos. Solar-Terrestrial Phys.*, *72*(14), 1068–1079. Retrieved from http://www.sciencedirect.com/science/article/pii/S1364682610001987 doi: https://doi.org/10.1016/j.jastp.2010.07.002

Klemm, J. (2019). *Classification and signal processing of radio backscatter from meteors* (Doctoral dissertation). Retrieved from http://hdl.handle.net/11122/10901

Kumar, G. K., & Hocking, W. K. (2010). Climatology of northern polar latitude MLT dynamics: Mean winds and tides. *Ann. Geophys.*, *28*(10), 1859–1876. doi: 10.5194/angeo-28-1859-2010

Lim, E.-P., Hendon, H. H., Butler, A. H., Garreaud, R. D., Polichtchouk, I., Shep-

herd, T. G., ... Nakamura, H. (2020). The 2019 Antarctic sudden stratospheric warming. *SPARC Newsl.*(54), 10–undefined.

Limpasuvan, V., Orsolini, Y. J., Chandran, A., Garcia, R. R., & Smith, A. K. (2016). On the composite response of the MLT to major sudden stratospheric warming events with elevated stratopause. *J. Geophys. Res. Atmos.*, *121*(9), 4518–4537. Retrieved from https://agupubs.onlinelibrary.wiley.com/doi/abs/10.1002/2015JD024401 doi: 10.1002/2015JD024401

Madden, R. A. (1979). Observations of large-scale traveling Rossby waves. *Rev. Geophys.*, *17*(8), 1935–1949. doi: 10.1029/RG017i008p01935

Manney, G. L., Krüger, K., Pawson, S., Minschwaner, K., Schwartz, M. J., Daffer, W. H., ... Waters, J. W. (2008). The evolution of the stratopause during the 2006 major warming: Satellite data and assimilated meteorological analyses. *J. Geophys. Res. Atmos.*, *113*(11), 1–16. doi: 10.1029/2007JD09097

Miyoshi, Y., & Yamazaki, Y. (2020). Excitation mechanism of ionospheric 6-day oscillation during the 2019 September sudden stratospheric warming event. *Earth Sp. Sci. Open Arch.*, 57. Retrieved from https://doi.org/10.1002/essoar.10503242.1 doi: 10.1002/essoar.10503242.1

Mo, X., & Zhang, D. (2020). Quasi-10-d wave modulation of an equatorial ionization anomaly during the Southern Hemisphere stratospheric warming of 2002. *Ann. Geophys.*, *38*(1), 9–16. doi: 10.5194/angeo-38-9-2020

Pancheva, D., Mukhtarov, P., Mitchell, N. J., Merzlyakov, E., Smith, A. K., Andonov, B., ... Murayama, Y. (2008). Planetary waves in coupling the stratosphere and mesosphere during the major stratospheric warming in 2003/2004. *J. Geophys. Res. Atmos.*, *113*(12), 1–22. Retrieved from http://dx.doi.org/10.1029/2007JD009011 doi: 10.1029/2007JD009011

Pedatella, N. M., & Forbes, J. M. (2010, jun). Evidence for stratosphere sudden warming-ionosphere coupling due to vertically propagating tides. *Geophys. Res. Lett.*, *37*(11), n/a–n/a. Retrieved from http://doi.wiley.com/10.1029/2010GL043560 doi: 10.1029/2010GL043560

Salby, M. L. (1982, nov). Sampling Theory for Asynoptic Satellite Observations. Part I: Space-Time Spectra, Resolution, and Aliasing. *J. Atmos. Sci.*, *39*(11), 2577–2600. Retrieved from https://doi.org/10.1175/1520-0469(1982)039{\%}3C2577:STFASO{\%}3E2.0.CO;2 doi: 10.1175/

463 1520-0469(1982)039⟨2577:STFASO⟩2.0.CO;2

464 Sassi, F., Garcia, R. R., & Hoppel, K. W. (2012). Large-Scale Rossby Normal Modes
465 during Some Recent Northern Hemisphere Winters. *J. Atmos. Sci.*, *69*(3),
466 820–839. doi: 10.1175/jas-d-11-0103.1

467 Siddiqui, T. A., Maute, A., & Pedatella, N. M. (2020). On the Importance of
468 Interactive Ozone Chemistry in Earth-System Models for Studying Mesophere-
469 Lower Thermosphere Tidal Changes during Sudden Stratospheric Warmings.
470 *J. Geophys. Res. Sp. Phys.*. Retrieved from `https://onlinelibrary.wiley`
471 `.com/doi/abs/10.1029/2019JA027193` doi: 10.1029/2019JA027193

472 Singer, W., Hoffmann, P., Kishore Kumar, G., Mitchell, N. J., & Matthias, V.
473 (2013). Atmospheric Coupling by Gravity Waves: Climatology of Grav-
474 ity Wave Activity, Mesospheric Turbulence and Their Relations to Solar
475 Activity. In F.-J. Lübken (Ed.), *Clim. weather sun-earth syst. highlights*
476 *from a prior. progr.* (pp. 409–427). Dordrecht: Springer Netherlands. Re-
477 trieved from `https://doi.org/10.1007/978-94-007-4348-9{\_}22` doi:
478 10.1007/978-94-007-4348-9_22

479 Siskind, D. E., Eckermann, S. D., McCormack, J. P., Coy, L., Hoppel, K. W., &
480 Baker, N. L. (2010). Case studies of the mesospheric response to recent mi-
481 nor, major, and extended stratospheric warmings. *J. Geophys. Res. Atmos.*,
482 *115*(20), 1–16. doi: 10.1029/2010JD014114

483 Stray, N. H., Orsolini, Y. J., Espy, P. J., Limpasuvan, V., & Hibbins, R. E. (2015).
484 Observations of planetary waves in the mesosphere-lower thermosphere during
485 stratospheric warming events. *Atmos. Chem. Phys.*, *15*(9), 4997–5005. doi:
486 10.5194/acp-15-4997-2015

487 Torrence, C., & Compo, G. P. (1998). A Practical Guide to Wavelet Analysis. *Bull.*
488 *Am. Meteorol. Soc.*, *79*(1), 61–78. doi: 10.1175/1520-0477(1998)079⟨0061:
489 APGTWA⟩2.0.CO;2

490 Yamazaki, Y. (2018). Quasi-6-Day Wave Effects on the Equatorial Ionization
491 Anomaly Over a Solar Cycle. *J. Geophys. Res. Sp. Phys.*, *123*(11), 9881–9892.
492 doi: 10.1029/2018JA026014

493 Yamazaki, Y., & Matthias, V. (2019). Large Amplitude Quasi-10-day Waves in the
494 Middle Atmosphere during Final Warmings. *J.Geophys. Res.*, 1–19. doi: 10
495 .1029/2019JD030634

Yamazaki, Y., Matthias, V., Miyoshi, Y., Stolle, C., Siddiqui, T., Kervalishvili, G., ... Alken, P. (2020). September 2019 Antarctic Sudden Stratospheric Warming: Quasi6Day Wave Burst and Ionospheric Effects. *Geophys. Res. Lett.*, *47*(1), 1–12. doi: 10.1029/2019GL086577

Yu, Y., Wan, W., Ning, B., Liu, L., Wang, Z., Hu, L., & Ren, Z. (2013). Tidal wind mapping from observations of a meteor radar chain in December 2011. *J. Geophys. Res. Sp. Phys.*, *118*(5), 2321–2332. Retrieved from `https://agupubs.onlinelibrary.wiley.com/doi/abs/10.1029/2012JA017976` doi: 10.1029/2012JA017976

Zhao, Y., Taylor, M. J., Pautet, P.-D., Moffat-Griffin, T., Hervig, M. E., Murphy, D. J., ... Russell III, J. M. (2019). Investigating an Unusually Large 28-Day Oscillation in Mesospheric Temperature Over Antarctica Using Ground-Based and Satellite Measurements. *J. Geophys. Res. Atmos.*, *124*(15), 8576–8593. Retrieved from `https://agupubs.onlinelibrary.wiley.com/doi/abs/10.1029/2019JD030286` doi: 10.1029/2019JD030286

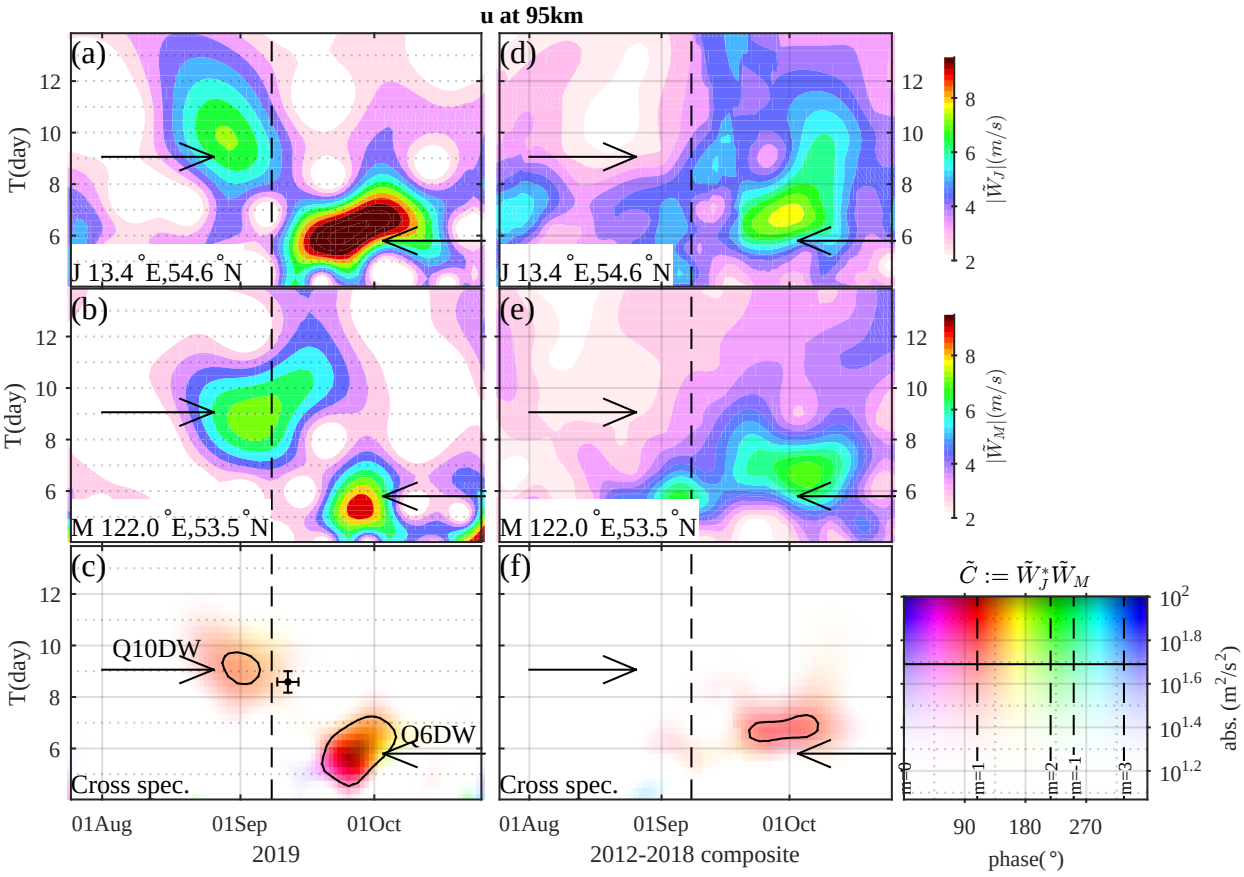

Figure 1: Wavelet spectra of the zonal wind at 95km altitude over the radar systems at (a) Juliusruh and (b) Mohe, and (c) their cross wavelet spectrum. In each Panel, the vertical dashed line represents the SH SSW onset; the horizontal arrows indicate the periods of the maxima of two peaks in (c). In (c), the color hue represents the phase difference between (a) and (b); the color hue is adjusted so that the redness denotes exactly m=1; the black isolines denote the amplitude $\sqrt{|\tilde{C}|}$=7 m/s; the horizontal error bar illustrates the temporal distribution of the USB- and LSB-like maxima indicated by the white crosses in Figures 2a-c, while the vertical bar illustrates the distribution of the estimated periods of RNM that can interact with SW2 and give rise to the maxima. (d,e,f) The same plots are (a,b,c) but from composite analyses between 2012 and 2017.

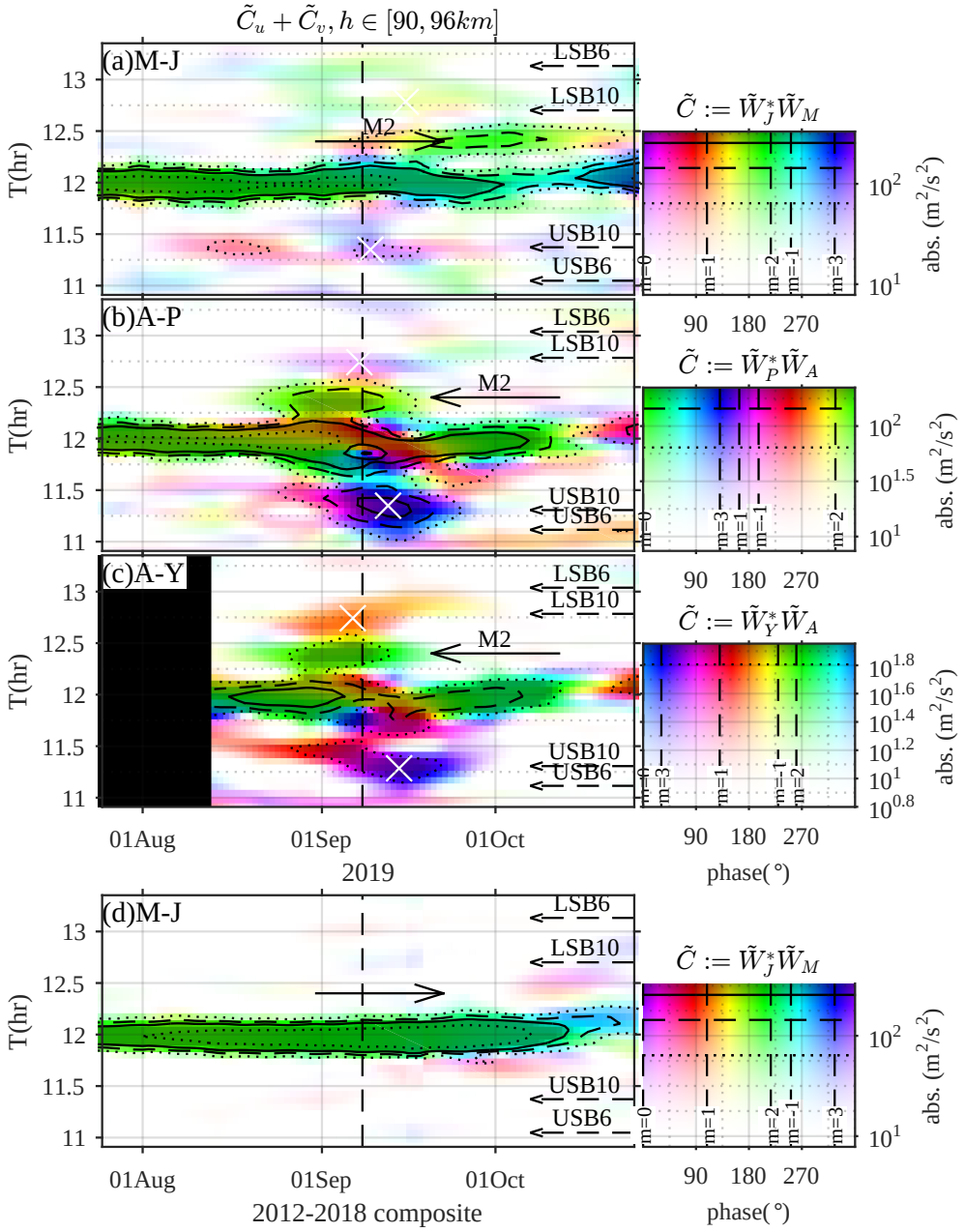

Figure 2: (a) Near-12hr CWL spectrum for the radar pair M-J, namely, similar plot as Figure 1c but summing the spectra of the zonal and meridional winds, averaged between 90 and 96km. All panels are adjusted so that blueness represents m=3. (b, c) Same plots as (a) but for the radar pairs A-P, and A-Y, respectively. (d) Same as (a) but for the 2012-2018 composite analysis. In each panel, the black isolines denote amplitudes at $\sqrt{|\tilde{C}|}$=8, 12, 16 and 24 m/s; the solid horizontal arrow indicates the M2-like signature; the dashed arrows on the most right-side illustrate the theoretical periods of the secondary waves (USB and LSB) of SW2-Q6DW and SW2-Q10DW nonlinear interactions; and the white crosses indicate local maxima of USB- and LSB-like peaks.

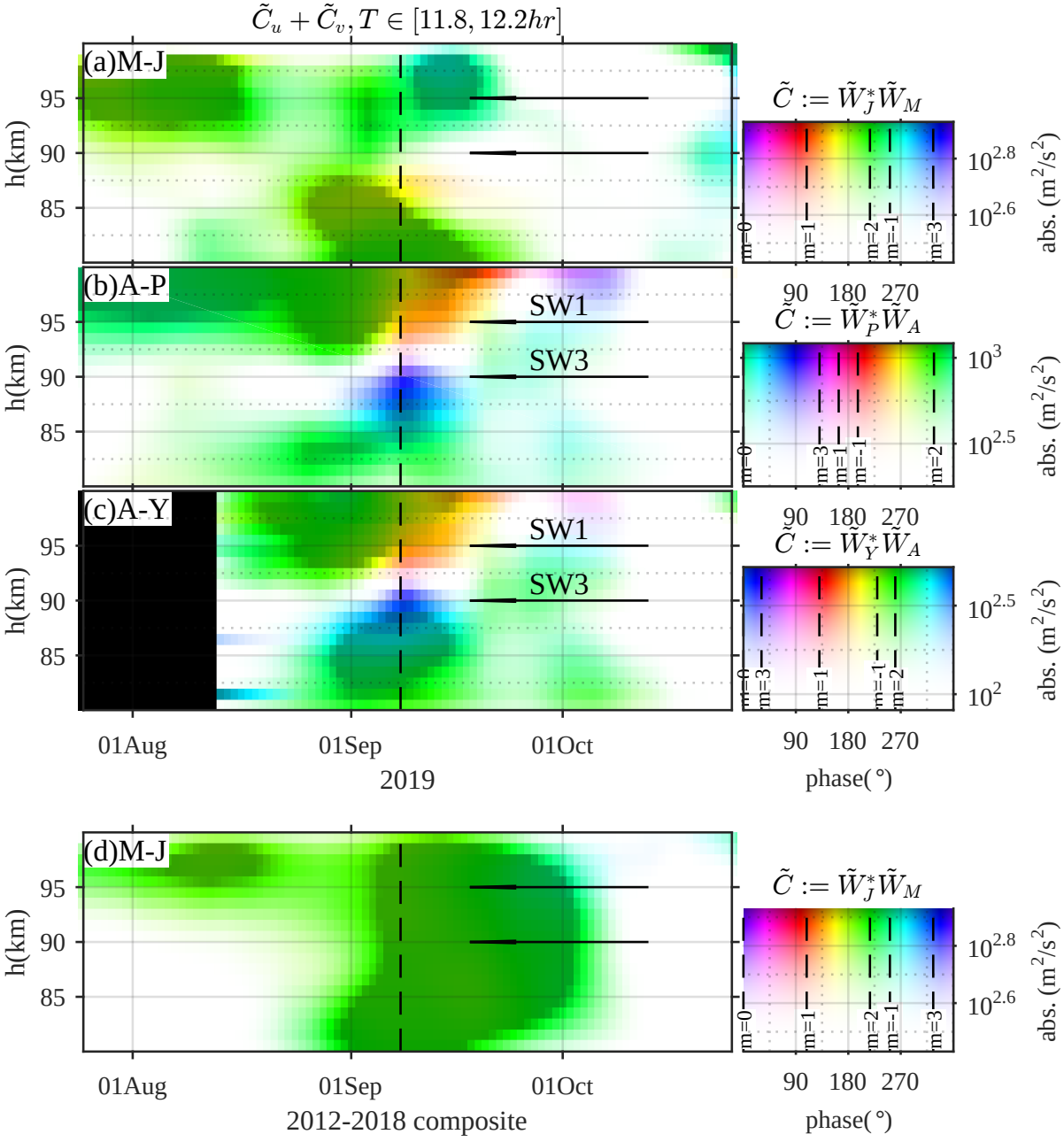

Figure 3: Same variable and panel arrangement as displayed in Figure 2 but as a function of date and altitude only at period T=12.0hr. For example, Panel (a) is combined from similar spectra as Figure 2a but at each individual altitude. The color is adapted so that green represents m=2. In (b,c), the horizontal arrows indicate SW1- and SW3-like signatures.

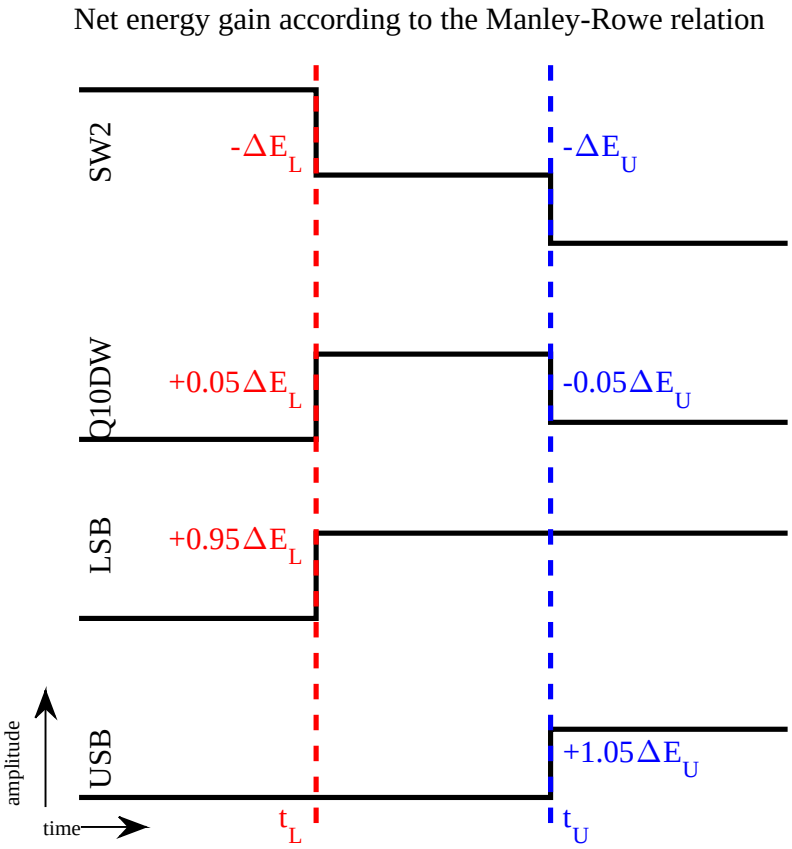

Figure 4: A sketch of net energy gain of the four waves in the Q10DW-SW2 nonlinear interactions according to the Manley-Rowe relation. The red and blue represent the LSB- and USB-generating interactions occurring at t_L and t_U, respectively. Between t_L and t_U maximizes the Q10DW. ΔE_L and ΔE_U are energy exchanged through SW2.

Appendix A Aliasing between Q6DW and the secondary waves of Q6DW-SW2 nonlinear interaction

Aliasing effects are intrinsic properties of all discrete signals. According to the Nyquist sampling theorem, a signal at frequency f_0, with a sampling frequency f_s and Nyquist frequency $f_N := f_s/2$, is indistinguishable from signals at $f = (Zf_s + f_N) \pm |f_0 - f_N|$ for all integers Z, and therefore they are aliases of each other. The largest near-zero distinguishable frequency range is $[0\ f_N)$. Readers are referred to Salby (1982) for a detailed description of the aliasing of the single-spacecraft approaches. Here, for a concise explanation, we consider a situation over the equator, where the temporal sampling interval of slowly precessing polar orbiter for a given longitude is about 12hr, or $f_s = 2\mathrm{d}^-$ and $f_N = 1\mathrm{d}^-$. A Q6DW signal at f_0 =0.2cpd is associated with aliases at f =1.8 and 2.2cpd, namely, the frequencies of the secondary waves of Q6DW-SW2 interactions. Note that this aliasing is independent from the coordinate systems. In the sun-synchronous coordinates system and for a given local time, f_s equals to the number of orbits per day (up to 15-16, e.g., in the case of Swarm) and f_N equals to 7.5-8cpd. However, the three waves are still indistinguishable because they are Doppler-shifted to the same frequency $|f| = 0.8$cpd. (A wave at f_0 in the earth-fixed frame is Doppler-shifted to f_S=f_0-m in sun-synchronous frames.)